Journal of Structural Geology 36 (2012) 2–15

Contents lists available at SciVerse ScienceDirect

Journal of Structural Geology

journal homepage: www.elsevier.com/locate/jsg

Electron backscatter diffraction analysis to determine the mechanisms that operated during dynamic recrystallisation of quartz-rich rocks

Angela Halfpenny*, David J. Prior [1], John Wheeler

Department of Geology and Geophysics, University of Liverpool, Liverpool, Merseyside L69 3GP, UK

ARTICLE INFO

Article history:
Received 30 April 2011
Received in revised form
23 November 2011
Accepted 9 January 2012
Available online 15 January 2012

Keywords:
Electron backscatter diffraction (EBSD)
Misorientation
Dynamic recrystallisation
Quartz
Deformation
Grain boundary sliding (GBS)

ABSTRACT

Determination of the controlling nucleation and recrystallisation mechanisms from a samples microstructure are essential for understanding how the microstructure formed and evolved through time. The aim of our research was to apply a quantified analytical approach to the identification of the controlling nucleation, recrystallisation and microstructural modification mechanisms. We used electron backscatter diffraction to quantify the microstructures of naturally deformed quartz-rich rocks which were deformed at various temperature and pressure conditions. Our results show that ratios of the recrystallised grain size to the subgrain size with values less than 1 (0.5–0.7 in the data presented here) suggest bulge nucleation, whereas ratios of ~1 suggest subgrain rotation nucleation. Other supporting evidence for subgrain rotation nucleation is an increase in misorientation from the centre of an original protolith 'parent' grain to the edge. All samples show evidence for modification of the microstructure due to grain boundary sliding including increased misorientation angles between grains and movement of recrystallised grains between parent grains. By systematically analysing sample microstructures it is possible to separate out evidence to determine the controlling nucleation and recrystallisation mechanisms, as well as being able to identify microstructure modification mechanisms. Using microstructural quantification via EBSD allows a systematic methodology to analyse samples from any location from an objective viewpoint.

1. Introduction

The microstructures of quartz rocks deformed by creep mechanisms are important as they can be used to interpret deformation processes and conditions (Bell and Etheridge, 1976; Lloyd and Freeman, 1994; Poirier and Guillope, 1979; Urai et al., 1986) in the Earth's crust. The pattern of quartz crystallographic preferred orientations (CPOs) (Schmid et al., 1986) can be used to constrain the conditions of deformation and the kinematic strain path. Recrystallised grain size can be used to estimate stress magnitudes (Ord and Christie, 1984; Stipp and Tullis, 2003; Twiss, 1986). An understanding of dynamic recrystallisation is crucial to understanding both CPO evolution and quantitative use of microstructures.

Dynamic recrystallisation processes are embedded in the concept of the three regimes of dislocation creep that have been identified from the microstructures of experimentally deformed quartz samples (Hirth and Tullis, 1992). Regime 1 represents lower temperatures, faster strain rates and the microstructure is characterised by inhomogenously deformed parent grains with patchy undulatory extinction and very fine recrystallised grains. Regime 2 represents increased temperature or decreased strain rate, the microstructure is characterised by flattened parent grains with sweeping undulatory extinction. The microstructure can show a core and mantle structure, and the recrystallised grain size is similar to the subgrain size of the parent grains. Regime 3 represents high temperature or low strain rate, and the microstructure is characterised by elongate parent grains with highly lobate boundaries and a high proportion of recrystallised grains.

The dominant recrystallisation mechanisms in regimes 1–3 have become a particular focus of attention (Stipp et al., 2002a). Strain-induced grain boundary migration (SIGBM) (Urai et al., 1986) and subgrain rotation recrystallisation (SGR) (Guillope and Poirier, 1979) are the two key processes identified as important in the dynamic recrystallisation of minerals. There is general consensus that regimes 1 and 3 are dominated by SIGBM, facilitated by a high driving force (dislocation density) or a high mobility (related to higher temperatures), respectively, and that regime 2 is dominated

* Corresponding author. Present address: CSIRO, Earth Science and Resource Engineering, ARRC, 26 Dick Perry Avenue, Kensington, Western Australia 6151, Australia. Tel.: +61 864368758; fax: +61 864368559.
E-mail address: angela.halfpenny@csiro.au (A. Halfpenny).
[1] Present address: Geology Department, University of Otago, 360 Leith Walk, Dunedin 9054, New Zealand.

0191-8141/$ – see front matter
doi:10.1016/j.jsg.2012.01.001

by SGR recrystallisation (G. Hirth personal communication). The nucleation mechanisms will control the initial recrystallised grain size and will influence the evolution of both rheology and CPOs. The SGR nucleation mechanism dominates in regime 2 and may also be an important nucleation mechanism in regime 3, creating new grains that can then grow by SIGBM (Urai et al., 1986). Since dislocation climb is difficult in regime 1 due to the low temperatures, SGR should not be an effective nucleation mechanism therefore nucleation is by grain boundary bulging. The relative roles of SGR and bulging for nucleation of recrystallised grains in each of the dislocation creep regimes have never been fully established.

Bestmann and Prior (2003) and Wheeler et al. (2003) suggested using the orientation of the recrystallised grains in relation to their parent grains as a tool to indicate nucleation mechanism. Nucleation via SGR or by bulging should both give rise to similar daughter and parent grain orientations and rational parent–daughter misorientation axes, which form the subgrain walls (Bestmann and Prior, 2003; Mariani et al., 2009). However many observations suggest that recrystallised grains tend to have high-angle misorientations to parent grains with non-rational, random misorientation axes (Bestmann et al., 2008; Bestmann and Prior, 2003; Halfpenny et al., 2006, 2004; Prior et al., 2004; Skemer and Karato, 2008; Storey and Prior, 2005). Such observations may relate to nucleation mechanisms that are not fully understood (Hobbs, 1968; Vernooij et al., 2006a; Wheeler et al., 2003) or to modification by twinning. However, a more common explanation is grain boundary sliding (GBS) which allows recrystallised grains to become dispersed throughout the microstructure with a weakening of the CPO strength (Bestmann et al., 2008; Bestmann and Prior, 2003; Halfpenny et al., 2006; Skemer and Karato, 2008; Storey and Prior, 2005) and randomisation of grain boundary misorientation axes (Jiang et al., 2000). It has been suggested that SGR leads to recrystallised grains which are (within error) the same size as the internal subgrains of the parent grain (Halfpenny et al., 2006; Stipp et al., 2010; Urai et al., 1986). In contrast bulging produces recrystallised grains which are smaller than the internal subgrain size (Halfpenny et al., 2006).

Automated electron backscatter diffraction EBSD (Prior et al., 1999) is critical to this work, because it allows quantification of the microstructure in terms of grain size, subgrain size, full crystallographic orientation and misorientation (Bestmann and Prior, 2003; Halfpenny et al., 2006; Pennock et al., 2006; Stipp and Kunze, 2008; Trimby et al., 1998; Valcke et al., 2006). Naturally deformed quartz aggregates representative of regimes 1–3 (Hirth and Tullis, 1992) have been chosen for this study. The aim of this research is to understand the nucleation mechanisms during dynamic recrystallisation of quartz. We reason that if microstructures can be quantified then they can be systematically compared regardless of location or deformation conditions. This will allow the determination of the controlling nucleation and recrystallisation mechanisms as well as defining microstructural modification mechanisms after nucleation and recrystallisation have taken place.

2. Samples

2.1. Regime 1 samples

Sample Stac B is a natural mylonitic quartzite collected from the Stack of Glencoul (Grid Ref. NC 28882876), in the Assynt region, NW Scotland. Callaway (1884) first described these rocks, which are now classed as S>L and L-S tectonites. The protolith for these rocks was a Cambrian quartzite, which was deformed by the Moine Thrust at greenschist facies conditions (Law et al., 1986, 2010). The sample was collected approximately 70 m below the Moine Thrust and exhibits 20% recrystallisation. The sample contains ~1% muscovite and is equivalent to sample SG15 of a previous study (Law et al., 1986).

Samples I2, I4 and I5a are from naturally deformed quartz veins from the Upper Val di Sole north of the Adamello/Presanella massif, Tonale Line (Eastern Alps, Italy), a dextral strike-slip segment of the Periadriatic fault system (Heitzmann, 1987; Schmid et al., 1989). The samples collected are from a 'natural laboratory', in which deformation occurs across a range of temperatures (250 °C–700 °C) related to the synkinematic Oligocene emplacement of the Presanella intrusion of the Adamello pluton (Stipp et al., 2004, 2002a). A constant confining pressure of 250–300 MPa and a strain rate of 10^{-11}–10^{-13}/s have been calculated for all Tonale Line samples (Stipp and Schmid, 1998; Stipp et al., 2002b). The main foliation dips 80° and strikes E–W to ENE–WSW, and a stretching lineation plunges on average at 12° towards 257°. Samples I2, I4 and I5a were deformed between 300 and 450 °C, estimated from metamorphic mineral assemblages of metasediments which host the veins (Stipp et al., 2002a,b).

2.2. Regime 2 samples

Sample CT210b is from the Sesia Zone, European Western Alps, lower Aosta valley, Italy (Grid Ref. 409.416°, 5043.720N) (Trepmann and Stockhert, 2003). The sample experienced a late stage of inhomogeneous deformation involving mylonitic shear zones with variable orientation, at temperatures of 300–350 °C (Kuster and Stockhert, 1999; Trepmann and Stockhert, 2003), fluctuating pore fluid pressures, very high stresses and correspondingly high stain rates of 10^{-11}–10^{-12}/s (Kuster and Stockhert, 1999; Trepmann and Stockhert, 2001, 2002). The sample contains ~99% quartz with a few white jadeite porphyroclasts. The sample consists of 35% recrystallised grains, between quartz ribbons.

Sample I10 is a naturally deformed quartz vein collected from the Tonale Line (see details in Section 2.1). It was deformed at ~500 °C, based on metamorphic mineral assemblages of metasediments which host the veins (Stipp et al., 2002a,b).

2.3. Regime 3 samples

Sample Stac A was collected at the Stack of Glencoul (see details in Section 2.1), 5 m below the Moine Thrust, from the white Cambrian quartz mylonites (Law et al., 1986). The sample is 65% recrystallised and contains approximately 1% muscovite. The sample is equivalent to sample SG10 of a previous study (Law, 1987; Law et al., 1986, 2010; Lloyd et al., 2010).

Samples I6, I7, I8, I9, and I11b were collected from naturally deformed quartz veins from the Tonale Line (see details in Section 2.1), and were deformed at 520–630 °C based on metamorphic mineral assemblages of metasediments which host the veins (Stipp et al., 2002a,b).

3. Analytical details

3.1. Sample preparation

Oriented rock samples were cut into slabs and areas of interest were selected. The billets for the thin section were oriented with lineation parallel to the long or short axis of the billet (Halfpenny, 2010). Standard XZ (parallel to lineation and perpendicular to foliation), 30 μm thick polished thin sections were chemically–mechanically polished using colloidal silica fluid (Lloyd, 1987) to remove surface damage. The thin section was given a thin carbon coat and the edges of the specimen surface were painted with conductive carbon paint to prevent charging. Sample

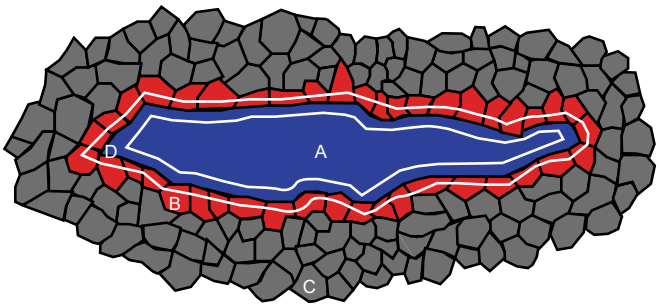

Fig. 1. Terminology diagram. (A) Original protolith grains are termed parents. (B) Recrystallised grains that are in contact with a parent grain are termed neighbour–daughters. (C) All other recrystallised grains, not in contact with a parent grain are termed daughters. (D) The data from only 1 μm either side of the parent to neighbour–daughters HAGB are termed edges.

analysis areas were selected using optical and electron microscopy using forescatter detectors to collect orientation contrast (OC) images (Prior et al., 1996). The chosen analysis regions were representative of the thin section's overall microstructure.

3.2. EBSD analytical conditions

Full crystallographic orientation data were gathered using automatically indexed EBSD patterns collected on either a CamScan X500 Crystal Probe SEM fitted with a field emission gun and a FASTRACK stage or a Philips XL30 SEM fitted with a tungsten filament. The EBSD patterns were collected using a 20 kV acceleration voltage and a beam current of 30 nA on the CamsScan and 3 nA on the Philips. The working distance was 25 mm and the angle between the specimen surface normal and the incident beam was 70°. Samples were mapped by moving the beam on a grid with a fixed step size of 2 μm and then moving the stage in-between each map. The step size was chosen ensuring that the recrystallised daughter grains and the subgrains contained ample (8–10) measurement points.

The EBSD patterns were indexed using the HKL Technology (now part of Oxford Instruments) manufacturer's software package CHANNEL (Schmidt and Olesen, 1989). Average measuring time was 0.2 s per point. The raw data have 51%–79% of pixels indexed as quartz. The non-indexed points correspond to grain boundaries, cracks and secondary phases.

3.3. Paper terminology

In this paper, grains are defined using EBSD data as areas enclosed entirely by high-angle grain boundaries (HAGB). In accordance with TEM data (Shigematsu et al., 2006; White, 1977) HAGBs have misorientations ≥10°. Subgrains are defined as areas enclosed entirely by low angle grain boundaries (LAGB) with misorientations ≥2° (Trimby et al., 1998). We have defined grain types based on their characteristics and location in the microstructure (Fig. 1). It is obvious from both optical and EBSD data that some grains are large, elongate, show internal deformation and highly serrated grain boundaries (Fig. 2): we interpret these as to be original protolith grains and refer to them as parent grains (Fig. 1). These were selected manually from the EBSD grain data. The remaining grains, i.e. those that are small and relatively strain-free, are interpreted as recrystallised grains and are termed daughter grains (Fig. 1). Daughter grains touching a parent grain (although not necessarily the parent grain from which they formed) are

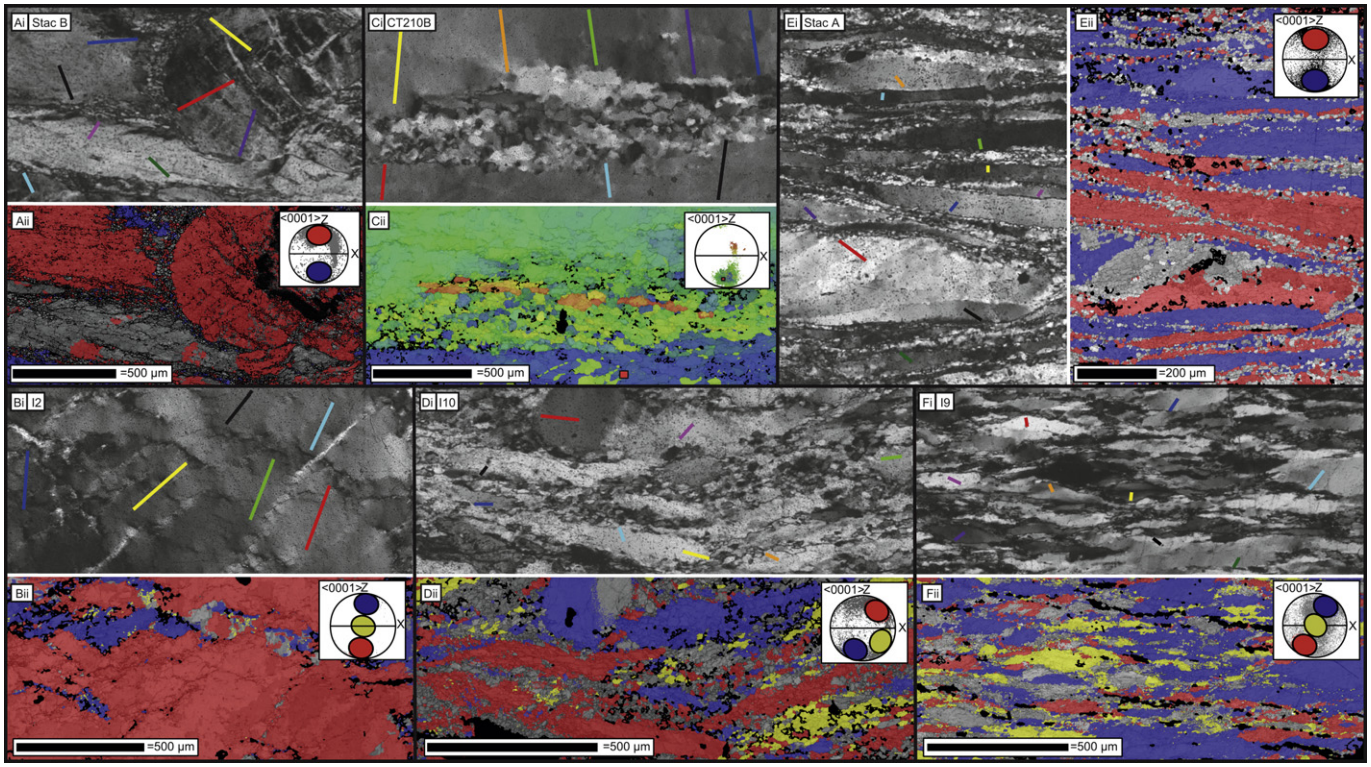

Fig. 2. Microstructural maps of Stac B, I2, CT210b, I10, Stac A and I9. Ai, Bi, Ci, Di, Ei, Fi are optical images of the area corresponding to the EBSD mapped area. The coloured lines marked on these images mark the locations of the misorientation profiles presented in Fig. 4. Aii, Bii, Cii, Dii, Eii, Fii are texture component maps coloured according to the pole figure key in the top right corner of each image. Aii, Bii, Dii, Eii, Fii component maps, grains are coloured if they are located within one of the defined orientation domains on the pole figures. Uncoloured grains are dispersed more than 30° away from the centre of a defined orientation domain. Cii texture component map plots misorientation angle variation from the chosen start location (red square marked on map and pole figure) up to a maximum misorientation of 104.5°.

Table 1
Microstructural information summary for all samples. Column 1, gives the sample code. Column 2, states the sample temperature (collated from other studies). Column 3, gives the percentage of the sample which is classed as recrystallised (neighbour–daughter + daughter grains). Column 4, states the calculated parent grain aspect ratio from EBSD maps or thin sections. Columns 5–8, show the statistically calculated average parent grain size, parent subgrain size, neighbour–daughter grain size and daughter grain size, respectively. Column 9, states the ratio of neighbour–daughter grain size to the subgrain size. Columns 10–12, give the calculated minimum, average and maximum orientation gradient within the first 20 μm of the parent grain edge. Column 13 shows the qualification of the overall appearance of the full length of the misorientation profiles. Column 14, states the interpreted regime (Hirth and Tullis, 1992).

Sample code	Temperature in °C	Quantity of recrystallised grains %	Parent aspect ratio	Average parent size in μm	Average subgrain size in μm	Average Neighbour–daughter size in μm	Average daughters size in μm	Ratio Neighbour–daughters/Subgrains	Minimum orientation gradient from edge of parent in degrees per micron	Average orientation gradient from edge of parent in degrees per micron	Maximum orientation gradient from edge of parent in degrees per micron	Overall misorientation parent profile gradient	Regime
I2	**300**	**15**	**2:1**	**94.9**	**21.7**	**13.5**	**13.8**	**0.6**	**0.1**	**0.2**	**0.3**	**Just fluctuates**	**1**
Stac B	**300–400**	**20**	**4:1**	**372.5**	**17.0**	**11.5**	**11.3**	**0.7**	**0.1**	**0.4**	**0.7**	**Just fluctuates**	**1**
I4	450	20	2:1	75.1	26.1	16.0	15.3	0.6	0.1	0.3	0.4	Just fluctuates	1
I5a	450	25	4:1	78.1	21.7	14.8	14.7	0.7	0.1	0.3	0.7	Just fluctuates	1
CT210b	**300–350**	**35**	**12:1**	**73.4**	**24.9**	**26.7**	**24.4**	**1.1**	**0.1**	**0.1**	**0.1**	**Increasing misorientation**	**2**
I10	**500**	**75**	**3:1**	**53.0**	**17.7**	**16.8**	**15.4**	**1.0**	**0.1**	**0.2**	**0.3**	**Increasing misorientation**	**2**
Stac A	**300–400**	**65**	**9:1**	**45.3**	**16.1**	**11.8**	**12.4**	**0.7**	**0.1**	**0.5**	**0.9**	**Just fluctuates**	**3**
I9	**520**	**45**	**3:1**	**28.7**	**15.5**	**11.5**	**11.3**	**0.7**	**0.1**	**0.4**	**0.6**	**Just fluctuates**	**3**
I11b	570	10	3:1	58.1	22.1	15.2	15.0	0.7	0.1	0.2	0.6	Just fluctuates	3
I8	570	10	3:1	93.9	27.3	13.0	13.1	0.5	0.1	0.3	0.6	Just fluctuates	3
I7	580	15	2:1	127.4	30.2	15.7	15.6	0.5	0.1	0.2	0.4	Just fluctuates	3
I6	630	20	2:1	105.2	37.5	17.0	16.5	0.5	0.1	0.2	0.3	Just fluctuates	3

referred to as neighbour–daughter grains (Fig. 1). A one pixel area either side of the defined parent HAGB is termed an edge (Fig. 1). The CHANNEL software allows data related to parent grains, neighbour–daughter grains, daughter grains and edges to be extracted from the set of all grains, so that the properties of each group can be analysed.

3.4. Data manipulation and presentation

Processing of raw data is required (Bestmann and Prior, 2003; Prior et al., 2009) in order to generate misorientation data (Wheeler et al., 2001) and ensure that grains and subgrains can be rigorously defined (Trimby et al., 1998). In particular isolated mis-indexed pixels need to be removed and non-indexed areas along grain boundaries and inside grains need to be filled with an orientation calculated from the surrounded indexed pixels. The processing procedures applied here are very similar to those outlined in Bestmann and Prior (2003). Given that non-indexed grain boundary regions are rarely more than one pixel wide we are confident that these procedures did not introduce significant artefacts or data biases.

Parental aspect ratios were measured either from the EBSD maps or from the thin section (when the EBSD maps did not contain the full parent grains, only sample CT210b). Grain and subgrain sizes are calculated as the diameter of a circle of equivalent area to the measured grain/subgrain area from the EBSD data. All grain size measurements will have a lower cut-off defined by the spatial resolution of the measurement technique. EBSD data are particularly problematic in this regard in that grains defined by a very small number of pixels can be an artefact of regions of poor indexing or systematic misindexing (Bestmann and Prior, 2003; Prior et al., 2009). For this reason we eliminated all grains smaller than four times the step size so that the lower size threshold in size distributions is 8 μm. Errors on the sizes of individual grains and subgrains are estimated to be the step size (2 μm). The generated grain data were exported from the CHANNEL software and the statistical calculations were performed in Microsoft Excel. Also, it must be noted that all size measurements are a minimum as no 2D sectioning technique recognises the actual size without stereological correction.

Orientation data are displayed on lower hemisphere, equal area pole figure projections, contoured pole figures are generated from the CHANNEL software using a contouring cone with a half width of 15°. Misorientation data are displayed as profiles, misorientation angle distribution histograms and angle/axis pair relationships. Misorientation profiles plot misorientation angle relative to the first point of the profile. Each profile plots from the centre of the parent grain and moves to the edge. The profile lengths vary due to the variable size of the parent grains. The misorientation angle distribution histograms show the relative frequency of misorientation angles. Relative frequency is the ratio of the observed frequency of some outcome and the total frequency of the random experiment. This is calculated for misorientation data between neighbouring points in a map. The misorientation angle distribution histograms plot 5° bins for angular relationships located (a) within parent grains only, (b) 1 pixel wide edges between parent grains and neighbour–daughters, (c) within and between all neighbour–daughter and daughter grains. Misorientation angle/axis pair relationships are displayed in the crystal reference frame on an inverse pole figure. The data were normalised to ±100 data points for each 10° angular plot so that the strength of the plots can be accurately compared. The data were contoured by the CHANNEL software using a contouring cone with a half width of 15°. Maximum and minimum stated for the contouring related to the multiples of uniform distribution.

4. Results

Table 1 summarises important microstructural parameters quantified using EBSD for all the samples. Of these 6 are illustrated in detail; Stac B, I2, CT210B, I10, Stac A and I9. These are representative samples of regimes 1, 2 and 3. In this section we indicate how each parameter provides insight, as follows.

4.1. Semi-quantitative strain indicators

4.1.1. Daughters %

This indicates how much recrystallisation has taken place.

4.1.2. Parent aspect ratio

This relates to finite strain; the shapes, though, will not be faithful indicators of the strain ellipse in the XZ plane because a) each grain will have been in a different initial orientation and b) once recrystallisation has commenced, parent grains and matrix may behave differently.

4.1.3. Average parent grain size

This is used for comparison with the subgrain size (see below).

4.2. New grain and subgrain sizes

4.2.1. Average subgrain size

This will be used to compare against the recrystallised grain sizes (see below, Table 1 and Fig. 3).

4.2.2. Average neighbour–daughter grain size

This is the average size of the new grains *adjacent to* the parent grains. We will argue that the difference between this and the average subgrain size (within parents) carries important information on recrystallisation mechanisms (see below, Table 1 and Fig. 3).

4.2.3. Average daughter grain size

This is the average size of all those new grains *not in contact with* a parent grain. We assume that these grains will have been in existence for longer than the neighbour–daughters and hence there *may* have been additional processes to modify their sizes.

4.2.4. Ratio of neighbour–daughter to subgrain size

Compares the average size of new grains in contact with any parent grain with the average internal subgrain size. We will argue that this measure can be used to determine the recrystallisation mechanism.

4.3. Crystallographic data

4.3.1. Orientation gradients at margins of parents

We explored the amount and pattern of plastic strain within the parent grains by examining misorientation profiles (Fig. 4). Each misorientation profiles start at the centre of the parent grain and approaches the edge, but all profiles have been plotted at the same scale covering a distance of 100 μm. The orientation differences between the edges of parent grains and positions 20 μm inside provide an indication of overall orientation gradient. We calculated average gradients over the first 20 μm on several profiles from each sample to gain some insight into the variability. Table 1 shows the minimum, average and maximum gradients from selected profiles from each sample. For example Fig. 4E shows 10 profiles from Stac A; the maximum gradient over the first 20 μm is 0.9°/μm (purple profile) whilst the average overall profiles is 0.5°/μm (Table 1). We also use the general form of the profiles in our interpretation. If recrystallisation is by subgrain rotation, we expect that there will be an increase in misorientation from core to margin of parent grains. If recrystallisation is by bulging, then there is no necessity for such an increase. The results show that for samples Stab B, I2, Stac A and I9 the profiles show random fluctuations whereas samples CT210b and I10 profiles which are increasing in misorientation (Fig. 4).

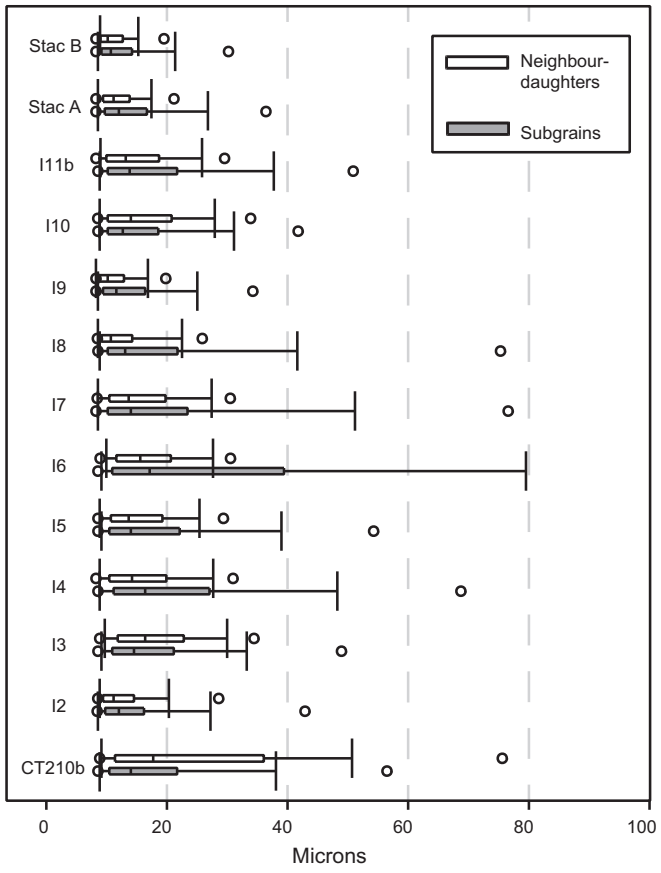

Fig. 3. Box and whisker plots showing the calculated neighbour–daughter grain size and the subgrain size for all samples. The whiskers plot the 5th to 95th percentile, left box edge plots 25th percentile, line in box plots 50th percentile, right edge of box plots 75th percentile of the size range. Open circles plot the measured minimum and maximum size values. There is no maximum size plotted for the subgrains for sample I6 as it was larger than 100 microns.

4.3.2. Orientation data

In all cases the parent grains are a small population and the CPOs shown here are not volumetrically representative. In all these samples the neighbour–daughter grains include the same orientation clusters seen in the parent grains, but show greater dispersion of the data and a reduction in CPO strength (compare maximum contour values for parent grains with neighbour–daughters on Fig. 5 and Table 2). In samples I2 and CT210B, a "new" orientation of neighbour–daughters close to the centre of the pole figure are seen, which does not correspond to the orientation of any of the parent grains (Fig. 5B and C). The orientation data for all samples are summarised in Table 2.

Pole figures do not illustrate the *spatial* distribution of grains with different orientations. To analyse the dispersion of orientations further, we defined orientation domains on the pole figures, showing c-axis orientations up to 30° from each of the original parent orientations (coloured insets on Fig. 6). An orientation domain with 30° spread was chosen as it captured the majority of parent grains of a particular orientation. Each EBSD analysis point was then colour-coded on a map (Fig. 6) in the same scheme as on

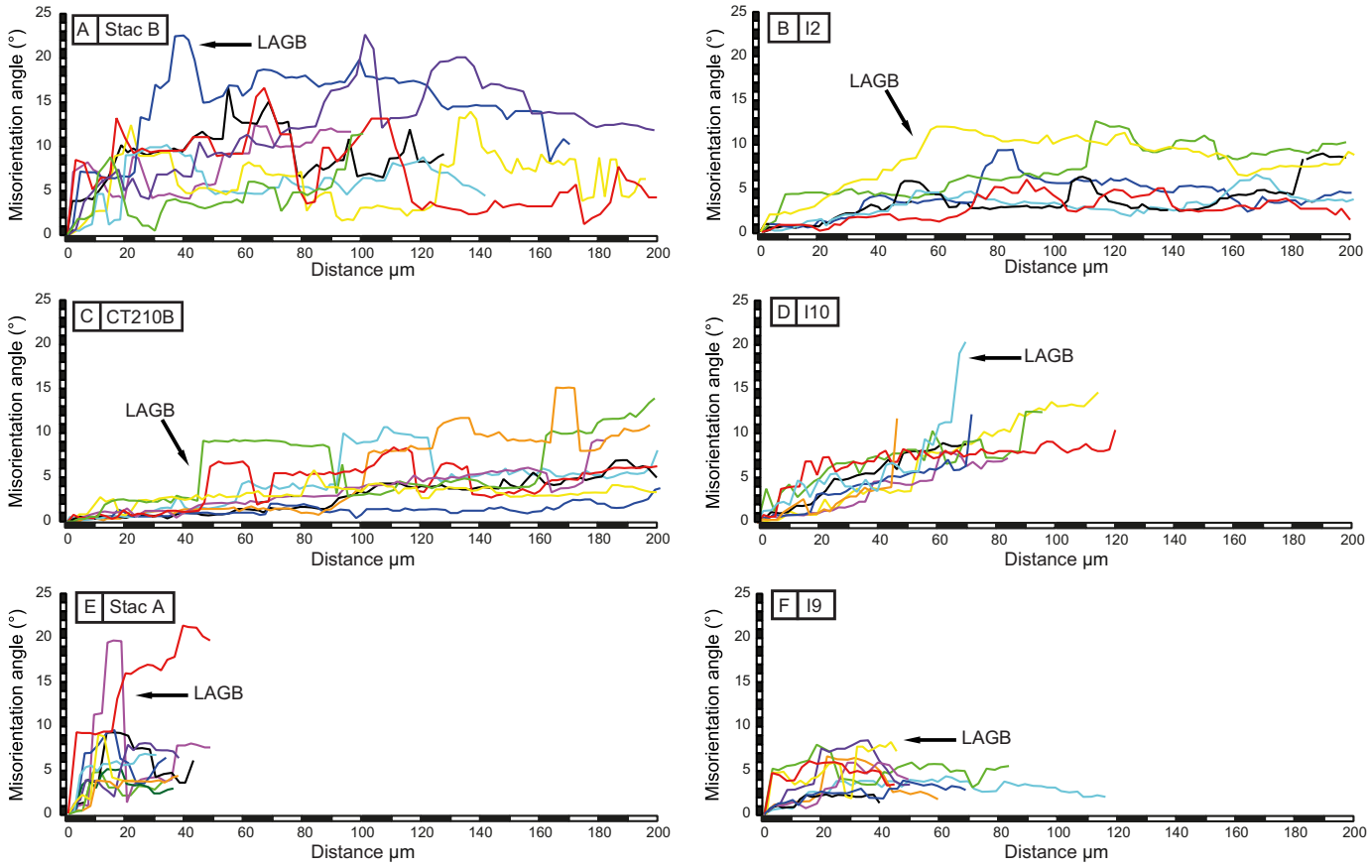

Fig. 4. Misorientation profiles of Stac B, I2, CT210b, I10, Stac A and I9 plotting misorientation relative to the first point on the profile, which means the misorientation is added up sequentially from the first point. Each transect is shown in a different colour and the locations are marked on Fig. 2 in corresponding colours. Some of the LAGBs have been marked onto the profile.

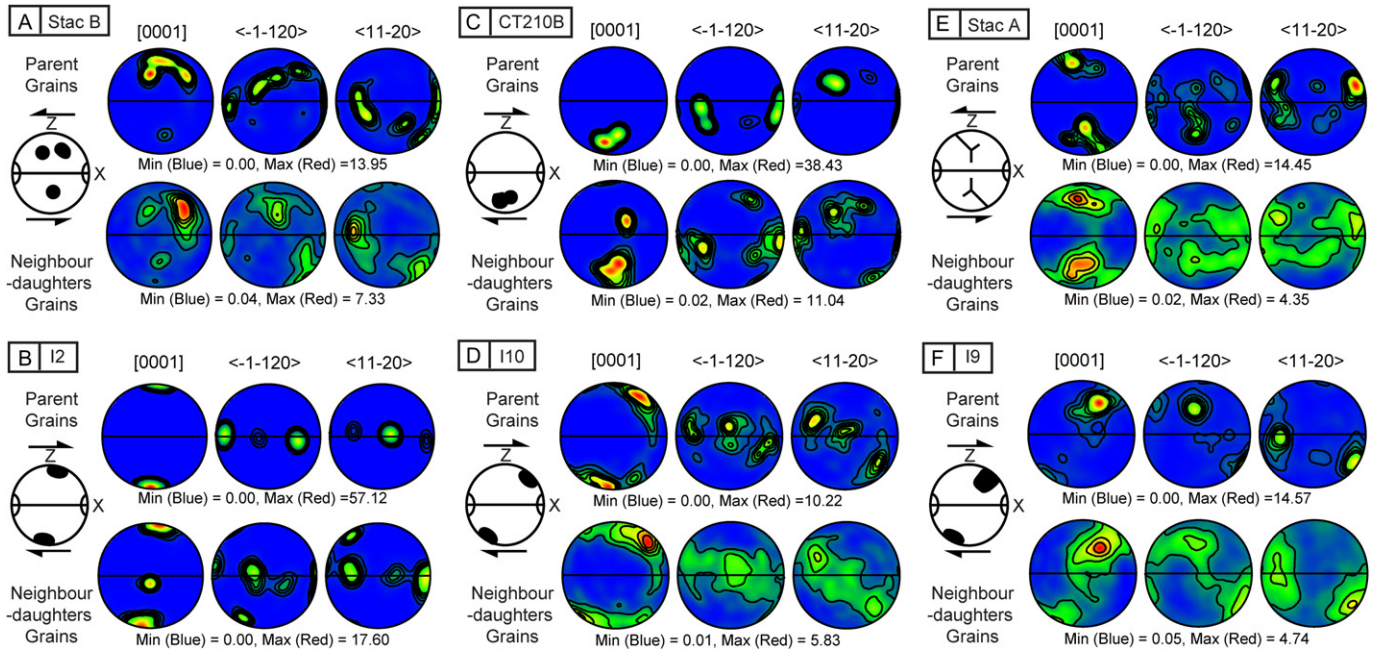

Fig. 5. Equal area, lower hemisphere, pole figures of Stac B, I2, CT210b, I10, Stac A and I9. The data were contoured using a contouring cone with a half width of 15°. The maximum and minimum numbers relate to the multiples of uniform distribution and show the strength of the texture. Top row: Parent grains only. Bottom row: Neighbour–daughter grains only. For each sample the data are summarised in a pole figure cartoon which shows the kinematic framework with foliation E–W and perpendicular to the page (Z = pole to foliation), lineation (×) horizontal within the foliation, and the shear sense indicated by arrows.

Table 2
Orientation data summary for all samples. Column 1, shows the sample code. Columns 2–5, state the texture style and strength for parent and neighbour–daughter grains. Column 6, provides a qualification of the relationship between the parent grains and neighbour–daughters. Column 7, is a description of the daughter grain relationships.

Sample code	Parent grains c-axis texture	Parent grains maximum texture strength	Neighbour–daughter grains c-axis texture	Neighbour–daughter maximum texture strength	Parent/Neighbour–daughter relationship	Daughter grains
I2	**Z cluster**	**57.12**	**More dispersed Z cluster + new Y cluster**	**17.60**	**Enclosed + next to**	**Located on lobate grain boundaries**
Stac B	**Z cluster**	**13.95**	**More dispersed Z cluster**	**7.33**	**Enclosed + next to**	**Located on lobate grain boundaries**
I4	Great circle or two clusters	37.72	More dispersed great circle or weaker two clusters	11.42	Enclosed + next to	Located on lobate grain boundaries
I5a	Strongly stretched Y cluster down towards Z	17.31	More dispersed Y cluster	10.30	Enclosed + next to	Located on lobate grain boundaries
CT210b	**Single bottom Z cluster**	**38.43**	**More dispersed Z cluster + new Y cluster**	**11.04**	**Next to other parent**	**Mixed orientations in matrix**
I10	**2× Z clusters**	**10.22**	**More dispersed Z clusters**	**5.83**	**Next to other parent**	**Mixed orientations in matrix**
Stac A	**Z cluster**	**14.45**	**More dispersed Z cluster**	**4.35**	**Next to other parent**	**Mixed orientations in matrix**
I9	**Z cluster**	**14.57**	**More dispersed Z cluster**	**4.74**	**Next to other parent**	**Mixed orientations in matrix**
I11b	Line of clusters/ single girdle	14.92	More dispersed line of clusters/single girdle	10.04	Next to other parent	Mixed orientations in matrix
I8	Z cluster	18.69	Slightly more dispersed Z cluster	6.22	Next to other parent	Mixed orientations in matrix
I7	Z cluster + weak X cluster	20.53	More dispersed Z + X clusters	6.29	Next to other parent	Mixed orientations in matrix
I6	Great circle	20.35	More dispersed great circle	9.42	Next to other parent	Mixed orientations in matrix

the pole figure. Uncoloured grains are dispersed more than 30° away from the centre of a cluster. The aim is to show how recrystallised grains with orientations close to parent grains are distributed around the sample. One might expect neighbour–daughter grains with a similar orientation to a particular parent to be in the vicinity of that parent. This is not always so – in all the maps, there are areas of the matrix where daughter grains from different orientation clusters are mixed (Fig. 6). Even daughter grains adjacent to a particular parent may have orientations corresponding more closely to that of another distant parent grain.

The texture component maps for samples Stac B and I2 highlight bulges (enclosed within yellow circles) which have formed on the boundaries of the parent grains and the neighbour–daughters orientations that are mixed between the parents (Fig. 6(Ai–Aiii) and (Bi–Biii)). The texture component map of CT210b was calculated by plotting the misorientation relative to a chosen point (red square on Fig. 2(Cii)) at the bottom edge of the map in the blue coloured parent grain, up to the maximum misorientation allowed (104.5°), using a rainbow colour scheme (Fig. 6(Ci–iii)). The bulk of the recrystallised grains show similar colours and are of the same orientation as the two parent grains; however the red coloured grains are misorientated between 80° and 104.5° from the two parent grains and represent the recrystallised grains of the second cluster of the pole figure (Fig. 5C).

4.3.3. Misorientation statistics

EBSD data enable the misorientations across all boundaries to be calculated and it is useful to display the statistics using histograms (Fig. 7). Consider first the histograms for within parent grains on Fig. 7, there is a peak which corresponds to LAGBs forming subgrain walls with misorientation angles of <10° (Table 3). We suggest that that the highest relative frequency misorientation angles represent early-formed LAGBs which have incorporated the most dislocations during recovery. After these angles the frequency of boundaries drop off and are lowest for boundaries with the misorientation angular range of 20–45°. The other main feature is a build up in frequency of boundaries to a sharp peak at 60° in every case (Fig. 7). Inverse pole figures confirm that the misorientation axis related to this peak is parallel to [c], and this peak may be due to Dauphiné twinning within the parents (Fig. 8) and all samples exhibit this twin relationship (Table 3).

The middle histograms for each sample of Fig. 7 represent the boundaries between the parent grains and the neighbour–daughter grains for a 1 pixel wide area either side of the parent grain HAGB. All of the plots exhibit a peak of LAGBs then the frequency of boundaries drop off to a lull around 30–40° and then increase to a second boundary angle peak at 60°, Dauphiné twins (Table 3). The frequency of boundaries then decreases again.

The third histogram on Fig. 7 describes the boundaries within and between the neighbour–daughter and daughter grains. The data exhibit a strong LAGB's peak, these boundaries are contained within the neighbour–daughter and daughter grains. Then there is a clear frequency decrease which reaches a minimum for misorientation angles in the range 25–40°. The frequency of boundaries exhibiting the angles then increases to a maximum at 60°.

Fig. 8 illustrates which crystallographic axis the data have been rotated about and by what angular relationship. All of the samples show the strongest maxima to correspond to a 60° rotation around the [c]-axis, this may be due to the formation of Dauphiné twins. The orientation of angles/axis pair relationships for <10° is controlled by the active slip systems moving the dislocations to form subgrain walls. As the slip systems active are dependent upon the deformation conditions of the sample this explains the variability shown in 2–10° plot. The plots 10–20°, 20–30°, 30–40°, 40–50° basically show a weakening of the strongest angles/axis pair relationship next to them, illustrating a modification of the strong LAGB and Dauphiné twin boundary relationships (Table 3).

5. Discussion

The sample microstructures have been described and characterised qualitatively and quantitatively using EBSD. The EBSD was used to: (1) characterise the CPO; (2) calculate the misorientation of the grain boundaries and internal substructure; (3) characterise the spatial relationship of the misorientation; (4) identify the parent, neighbour–daughter and daughter grains; (5) calculate the average parent grain aspect ratio; (6) quantify the internal subgrain size of the parents; (7) quantify the average grain size of the neighbour–daughters; and (8) calculate the misorientation angle/axis pairs. Due to the quantification of the sample microstructures it is possible to numerically compare the results. The data can be

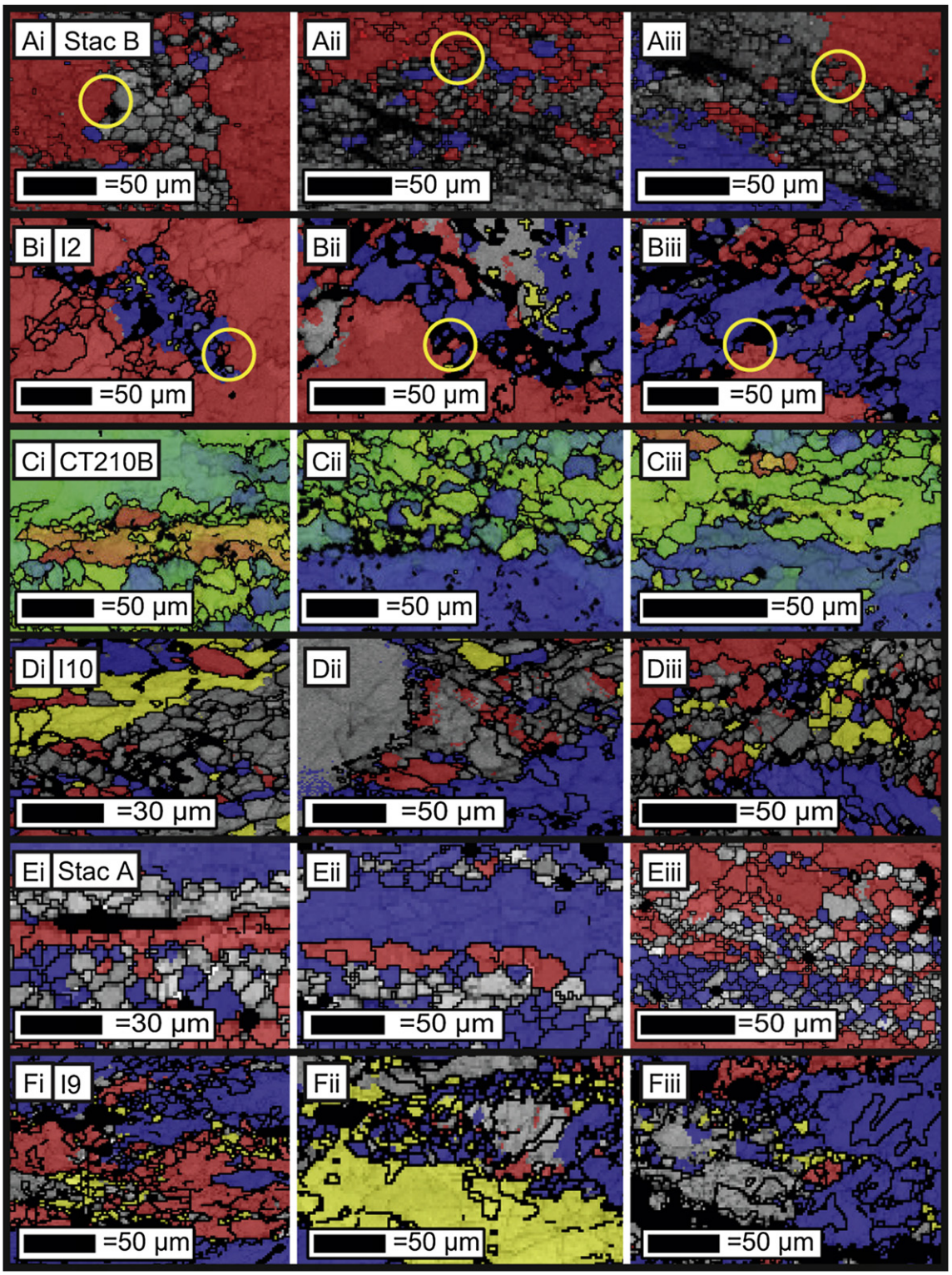

Fig. 6. Highlighted texture component map areas from the maps presented in Fig. 2 of Stac B (Ai, Aii, Aiii), I2 (Bi, Bii, Biii), CT210b (Ci, Cii, Ciii), I10 (Di, Dii, Diii), Stac A (Ei, Eii, Eiii) and I9 (Fi, Fii, Fiii). Each panel illustrates mixed orientations (different coloured grains next to each other) and grain boundary bulges (highlighted by yellow circles). How the maps are produced is explained in the text and in Fig. 2.

used to support a microstructural interpretation concerning the controlling nucleation and recrystallisation mechanisms active during deformation. We now discuss how the different types of data relate to deformation and recrystallisation mechanisms. Fig. 9 gives a schematic summary of the different types of microstructure.

5.1. Subgrain rotation recrystallisation (SGR)

SGR involves the glide and climb of dislocations to initially form LAGBs or subgrain walls. With further deformation and recovery, more dislocations are moved into the subgrain wall which causes an

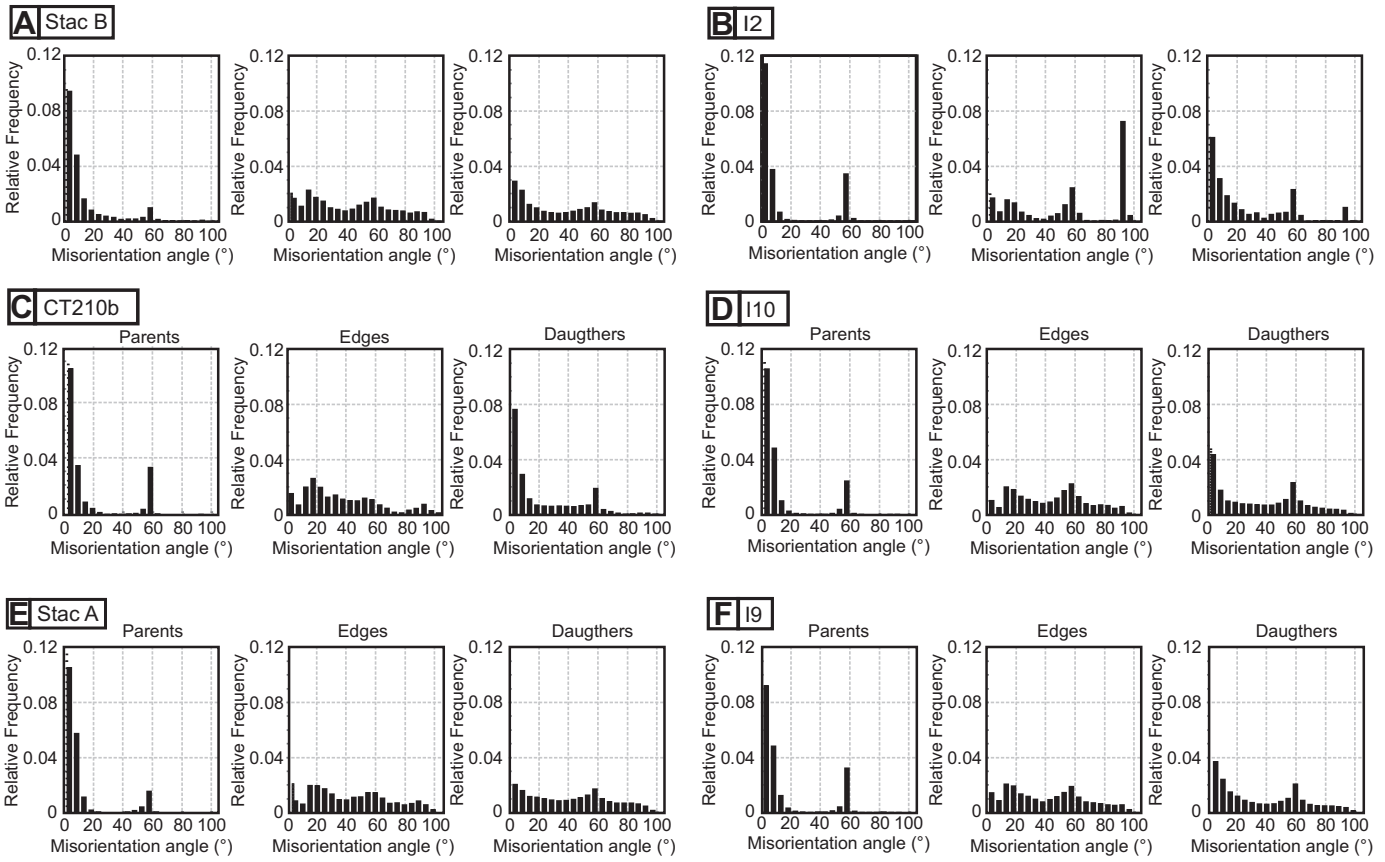

Fig. 7. Misorientation angles of Stac B, I2, CT210b, I10, Stac A and I9 plotted as relative frequency histograms calculated for neighbouring pixels. The first histogram plots misorientation angles between neighbouring pixels inside the parent grains. The middle histogram plots data only from the edges. The third histogram plots the relationships for neighbour–daughters and daughter grains (all recrystallised grains).

increase in the misorientation between the two sections of lattice, and thus rotation of the subgrain. As this process continues the misorientation angle between the parent grain and the subgrain slowly increases until it reaches a critical angle (10° for quartz (Shigematsu et al., 2006; White, 1977)). At this point the structure of the boundary changes and so does the boundary's classification from an LAGB to a HAGB. If SGR is the controlling nucleation mechanism the recrystallised daughter grains should be of a similar size to the internal subgrains of the parent grain (Urai et al., 1986). Also the range of grain sizes should be similar between the subgrains and neighbour–daughter grains. SGR recrystallisation is characterised by grains with very similar dislocation densities (Tullis et al., 1990).

The microstructures of CT210b and I10 are consistent with SGR as the dominant recrystallisation mechanism (Fig. 9B) because:

(1) recrystallised neighbour–daughter grain size is the same as the internal subgrain size of the parents (Table 1);
(2) the range of subgrain and neighbour–daughter grain sizes is similar (Fig. 3); and
(3) misorientation increases from the centre of the parent grains to the edge (Fig. 4, Table 3), they show core and mantle structure (Gifkins, 1976) illustrated by White (1976) which is characteristic of SGR (Hirth and Tullis, 1992).

5.2. Driving force for strain-induced grain boundary migration recrystallisation (SIGBM)

SIGBM occurs by the movement of a grain boundary from one parent grain into another, the pinching off of a boundary bulge, nucleates a new recrystallised grain. SIGBM can begin by bulge nucleation (Bailey and Hirsch, 1962), a distinctive feature of bulge nucleation in dynamic recrystallisation is that while several boundaries of a new grain may be established by grain boundary migration, full isolation of the grain may commonly be achieved by the development of a bridging subgrain boundary and its conversion by progressive SGR into a grain boundary (Urai et al., 1986). SIGBM can be facilitated by high driving force (dislocation density difference) or by high mobility (higher temperature) depending upon the deformation conditions.

5.2.1. SIGBM due to high driving force

Evidence for SIGBM due to a high driving force includes a strongly variable dislocation density and the presence of highly irregular grain boundaries. The irregular boundaries are caused by the creation of bulges and transfer of material across the grain boundaries. The areas that bulge will tend to have relatively low internal strain energy and consume areas of high internal strain energy, producing a relatively strain-free new grain. The bulge size is not controlled by the subgrain size of the parent but the difference in dislocation density between the grains and bulge growth can be maintained whilst this driving force exists. Because the parental internal subgrain size does not control the recrystallised neighbour–daughter grain size, the neighbour–daughter grain size range is independent of the subgrain size range. New grains can also develop along deformation bands (Etheridge and Hobbs, 1974) and other areas of high dislocation density which allow the lattice to become sufficiently misorientated for a HAGB to develop (White, 1976).

Table 3
Misorientation data summary for all samples. Column 1, shows the sample code. Columns 2–4, show the misorientation angular range with the largest relative frequency for boundaries within parent grains, within the edges and between/within neighbour–daughter and daughter grains (recrystallised grains). Columns 5–7, give the percentage of boundaries with misorientation angles >10°. Columns 8–13, state the crystallographic locations which the data are clustered around for particular misorientation angular ranges. Column 14, shows the angular range which exhibits the weakest texture strength.

Sample code	Parents highest relative frequency angle	Edges highest relative frequency angle	Daughters highest relative frequency angle	Parent % boundaries >10°	Edges % boundaries >10°	Daughters % boundaries >10°	Dominant axis 2–10°	Dominant axis 10–20°	Dominant axis 20–30°	Dominant axis 30–40°	Dominant axis 40–50°	Dominant axis 50–60°	Weakest axis
I2	**2–5**	**90–95**	**2–5**	**23%**	**87%**	**53%**	**<m> + weak [c]**	**<m> + weak [c]**	**[c] + <m>**	**[c] + weak <a>**	**[c]**	**[c]**	**10 to 20**
Stac B	**2–5**	**10–15**	**2–5**	**26%**	**87%**	**71%**	**[c]**	**[c]**	**[c] + <r>**	**[c] + <r>**	**[c]**	**[c]**	**10 to 20**
I4	2–5	55–60	2–5	35%	93%	64%	[c]	[c] + weak <m>	<m>	[c] + <m>	[c]	[c]	20–30
I5a	2–5	55–60	2–5	32%	92%	56%	[c]	[c]	[c] + weak <m>	[c]	[c]	[c]	20–30
CT210b	**2–5**	**15–20**	**2–5**	**27%**	**89%**	**45%**	**[c]**	**[c]**	**weak [c]**	**weak [c]**	**[c]**	**[c]**	**30–40**
I10	**2–5**	**55–60**	**2–5**	**21%**	**93%**	**69%**	**<π′>**	**weak [c] + weak <m>**	**[c] + weak <a>**	**[c]**	**[c]**	**[c]**	**10 to 20**
Stac A	**2–5**	**10–15**	**2–5**	**16%**	**93%**	**81%**	**[c]**	**[c]**	**[c] + <a>**	**[c]**	**[c]**	**[c]**	**20-30**
I9	**2–5**	**10–15**	**2–5**	**28%**	**89%**	**69%**	**[c]**	**[c] + weak <π>**	**[c] + weak <π>**	**[c]**	**[c]**	**[c]**	**10 to 20**
I11b	2–5	55–60	2–5	41%	94%	62%	[c]	weak [c] + weak <m>	[c] + <m>	[c] + <m>	[c]	[c]	10 to 20
I8	2–5	55–60	2–5	45%	90%	44%	[c]	[c]	[c]	[c]	[c]	[c]	10 to 20
I7	2–5	10–15	2–5	33%	94%	54%	[c]	[c] + weak <a>	[c] + weak <p>	[c] + weak <z>	[c]	[c]	20–30
I6	55–60	55–60	55–60	64%	88%	57%	[c]	[c] + <a>	[c] + <a> + <m>	[c] + <m>	[c] + <m>	[c]	40–50

Samples Stac B, I2, I4 and I5a provide evidence for recrystallisation by SIGBM facilitated by high driving force (Fig. 9A) because:

(1) the parent grains exhibit highly serrated grain boundaries (Fig. 2);
(2) the neighbour–daughter grains exhibit little internal deformation (Fig. 2);
(3) subgrains and neighbour–daughter grains are not the same size (Fig. 3, Table 1);
(4) the size ranges of subgrains and neighbour–daughter grains are different (Fig. 3); and
(5) no increase in misorientation from the centre of the parent grains to the edges (Fig. 4, Table 3).

5.2.2. SIGBM due to high mobility

Evidence for SIGBM due to a high mobility includes the presence of highly irregular grain boundaries and the development of a large portion of recrystallised grains. A large proportion of recrystallised grains can be produced as the driving force has not been depleted. The irregular boundaries are caused by the movement of the HAGB of a parent grain due its high mobility. As for SIGBM due to a high driving force the bulge size and recrystallised size range are independent of the subgrain size of the parent.

Samples Stac A, I9, I11b, I7, I8 and I6 evidence which supports recrystallisation via SIGBM due to high mobility for (Fig. 9C) are:

(1) all parent grains show highly serrated boundaries (Fig. 2);
(2) neighbour–daughters with very little to no internal deformation (Fig. 2);
(3) the misorientation angles inside the parent grains do not increase from the centre of the grain to the edge (Fig. 4, Table 3);
(4) the subgrain size and the neighbour–daughter grain size are not similar (Fig. 3, Table 1);
(5) the subgrains and neighbour–daughter grain size ranges are different (Fig. 3); and
(6) all samples have a large proportion of recrystallised grains which are multiple layers thick (Figs. 2 and 6, Table 1).

5.2.3. Controls on bulge size

The bulge size could be restricted by impurities in the sample pinning the boundaries of the growing bulge. This could be possible for limiting the size of a few bulges but could not have affected all bulges as it would require each sample to have impurities which are evenly spaced throughout the microstructure to cause the pinning. None of the microstructures showed an even distribution of impurities (Fig. 2), although the few impurities which do exist may contribute to grain boundary pinning. Another possible method of restricting the bulge size is removal of the driving force for SIGBM; the bulges can only keep growing so long as they maintain a critical dislocation density difference or the boundaries have high mobility. It may also be possible that the driving force behind bulge growth can only sustain bulges up to a specific grain size before the bulge has been converted into a new grain. The end size of the bulge could simply be a function of how long the bulges have to grow before the bridging subgrain boundary angle increases sufficiently to convert the bulge into a recrystallised grain.

5.3. Processes of increasing the misorientation angle

The nucleation and recrystallisation mechanisms discussed above would all create grain boundaries with misorientation angles

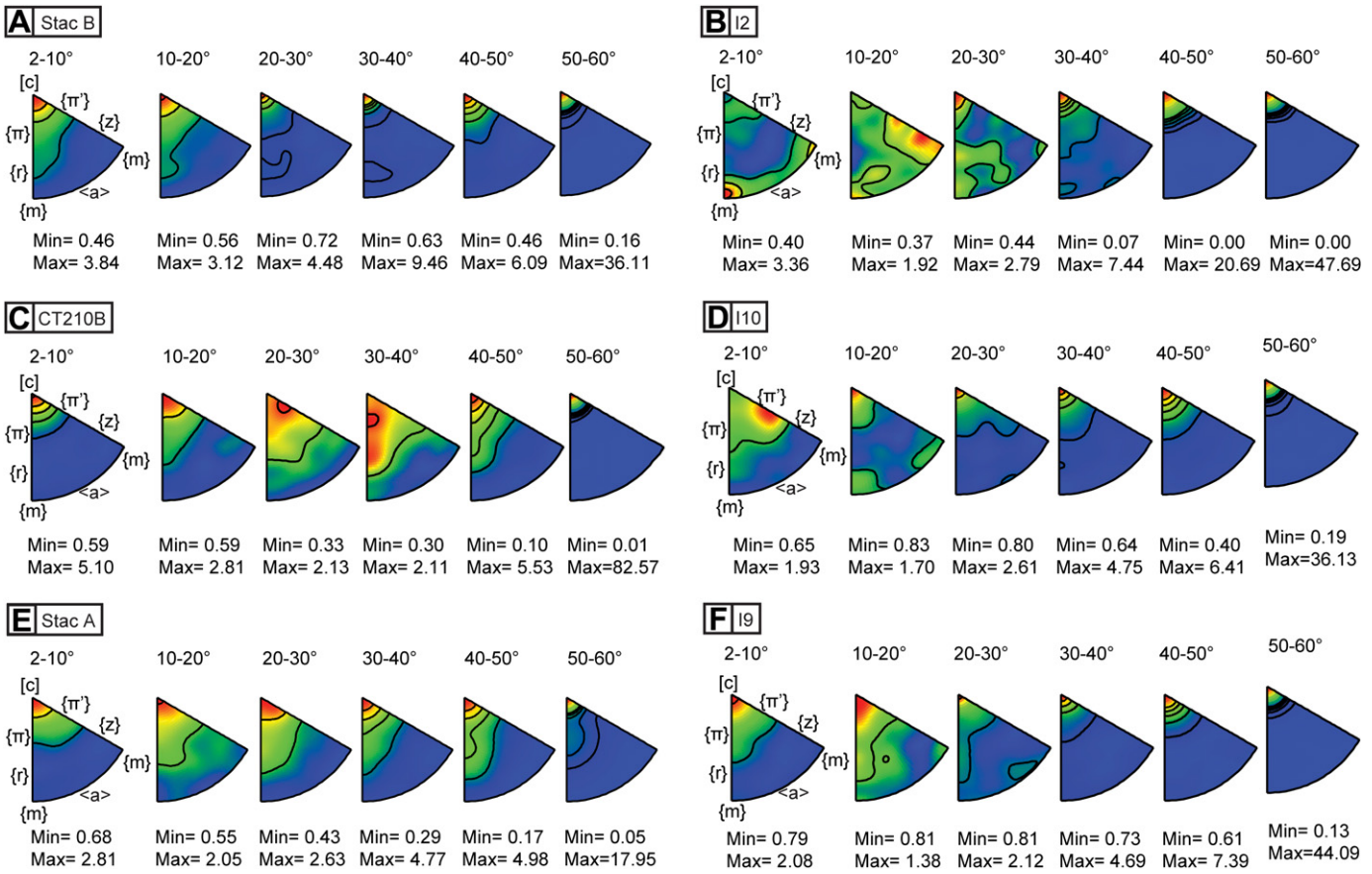

Fig. 8. Comparison of neighbouring misorientation axis and angles plotted in crystallographic coordinates on 10° interval inverse pole figures for Stac B, I2, CT210b, I10, Stac A and I9. Each triangle presented for the same sample contains ±100 data points, this allows the texture strength (max and min values) to be directly compared. The data were contoured using a contouring cone with a half width of 15°. The locations of important crystallographic axes are marked on the first plots and are the same for all plots.

of 10° (when LAGB turns into a HAGB). Table 3 lists the most abundant misorientation angles between the parent grains and neighbour–daughters, as well as the angles between the neighbour–daughters. There is a lot of variation in the misorientation angle ranges, from 10 to 15° up to 90 to 95°. Some samples show a peak misorientation range of 10–15°, but for all samples at least 50% of the grain boundaries between parent and neighbour–daughter grains have misorientation angles of >30° (Table 3).

Following nucleation, any rotation without crystallographic control would randomise misorientation axes (Jiang et al., 2000). The amount of weakening of the CPO would be dependent upon the strength and length of time that the mechanism controlling the rotations persisted. Initial strain-induced bulging occurs between original parent grains. After the formation of neighbour–daughter grains between the two parents, subsequent bulging will be between these neighbour–daughter grains and the parents. One might argue that the degree of CPO dispersion observed could be generated by the progressive misorientation as each new 'layer' is formed. However, single grain wide layers between two parents show as much dispersion as thicker bands of daughter grain (Figs. 2 and 6).

Other mechanism(s) must have acted upon the neighbour–daughter grains to increase their misorientation after nucleation. In Table 2 the spatial relationships of the interpreted neighbour–daughter grains and daughter grains are summarised. Assuming that each neighbour–daughter grain has recrystallised from a parent of a similar orientation, these columns highlight movement of the neighbour–daughter grains between parent grains, and their incorporation with other orientations of the recrystallised matrix. There are two microstructural modifications that need to be explained: (1) the increased misorientation angles between grains, and (2) spatial mixing of recrystallised grain orientations. It is important to remember that a thin section is a 2D view of a 3D aggregate and a recrystallised daughter grain which in a map view of the thin section is not close to any parent grain could be right next to one in the third dimension.

There are a few possible methods for increasing the misorientation between grains, including brittle deformation, twinning, and GBS.

5.3.1. *Continued plasticity and movement of dislocations into HAGBs*

Continued rational rotation of boundaries cannot be achieved by continuing to add dislocations into the boundary, once a HAGB structure has been developed. The Hall-Petch theory states that grain boundaries constitute an obstacle to dislocations and as they pile up behind the grain boundary, the stress concentration at the tip of the slip plane increases and will eventually cause the grain boundary to yield. When this happens deformation is transferred to the next grain, not the grain boundary (Hall, 1951; Petch, 1953).

5.3.2. *Cataclasis*

Some shear zones may initiate along planar microcracks and further microcracking results in a cataclastic shear zone (Vernooij et al., 2006b). In this situation new grains can develop by the rotations of rigid rock fragments, and the rock can then be overprinted by a phase of plastic deformation. It is possible that there was some early brittle deformation in our samples, but it is unlikely

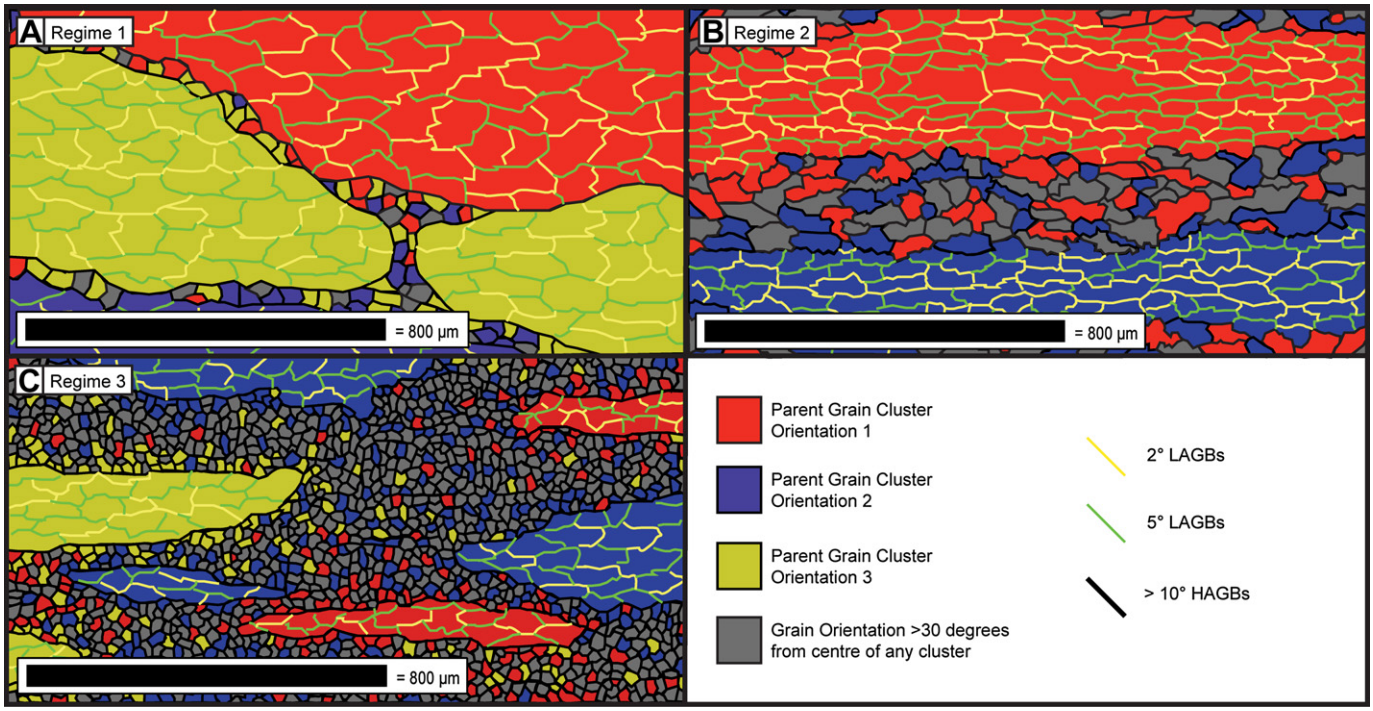

Fig. 9. (A) Regime 1 samples summary diagram (samples Stac B, I2, I4 and I5a), which shows the misorientation of parental subgrain boundaries to be randomly arranged. The internal subgrain size is larger than the neighbour–daughter grain size. There is limited development of recrystallised grains. Some recrystallised grains adjacent to each parent exhibit orientations similar to the parent grains. (B) Regime 2 samples summary (samples CT210b and I10) shows the development of core and mantle structure. The internal subgrain size is approximately the same size as the neighbour–daughters. Some neighbour–daughters show orientations similar to the parent grains. (C) Regime 3 samples summary diagram (samples Stac A, I9, I11b, I8, I7, I6) of the microstructure data showing the misorientation does not gradually increase from the centre of the parent grain. The internal subgrain size is larger than the neighbour–daughter grain size. There is the development of a large proportion of recrystallised grains and some exhibit orientations similar to the parent grains.

that there would be no preservation of this brittle event. To check for brittle deformation evidence the samples were imaged using cathodoluminescence and no textures which are characteristic of brittle deformation were noted. Therefore we ruled out brittle processes as a possible mechanism in these samples for increasing the misorientation angles.

5.3.3. Twinning

Dauphiné twins (180° rotation about 0001, the [c] axis, shows up as a 60° rotation due to symmetry in EBSD data) cause dramatic increases in the misorientation angle and every sample analysed shows the presence of Dauphiné twins (Table 3) (Menegon et al., 2011). The Dauphiné twins are dominant in the misorientation angle/axes of 50–60° in pair data analyses, where the plots always exhibit an extremely strong cluster about the [c] axis (Fig. 8). The misorientation angle/axis pair plots for each of the samples tend to show strong clustering for the LAGBs and Dauphiné twins. There are other twin laws besides Dauphiné (Kruhl and Peternell, 2002; McLaren, 1986) which are rarer (Japan Law) or cannot be recognised by diffraction data (Brazil) (Friedel, 1923). These other twins may also be important for increasing the misorientation angles (Vernooij et al., 2006a). Thus twinning is a mechanism capable of forming HAGBs but only specific angles which relate to the twin law. Any rotation necessary to cause higher or lower angles would have to be performed by another mechanism.

5.3.4. Grain boundary sliding (GBS)

GBS is a mechanism which is capable of accommodating intergrain incompatibility (Zhang et al., 1996). GBS can also cause neighbour switching, which can result in spatial mixing of the grains. GBS can be mechanical, frictional or diffusion accommodated; a small amount of GBS can actually enhance fabric (CPO) development but increased or dominant GBS will weaken the fabric (Zhang et al., 1994). GBS becomes faster as the boundaries become geometrically simplified (Gifkins, 1976). The following features have been used as evidence of dominant GBS: (1) square and rectangular grains; (2) smooth straight grain boundaries; (3) voids along the grain boundaries especially at triple junctions; and (4) alignment of groups of grains to form planes of grain boundaries parallel to mylonite foliation (White, 1977, 1979). Another criterion for the operation of dominant GBS is that the recrystallised grain size (neighbour–daughter and daughter grain size) is smaller than the stable subgrain size for a given temperature and stress (Ball, 1997; Ball and Hutchinson, 1969; Mohamed and Langdon, 1976; White, 1979). Many of our samples exhibit a recrystallised neighbour–daughter grain size which is smaller than the subgrain size of the parents, suggesting the operation of GBS.

The microstructural evidence for GBS from the samples includes the alignment of secondary phases along grain boundaries, and the polygonal shapes of the recrystallised grains (Fig. 2). The misorientation axis data for the LAGB (plots of 2–10°) exhibit strong clustering, but the strength of the clusters always decreases above 2–10° and the plots for 10–20° and 20–30° tend to exhibit the weakest clustering values (Table 3, Fig. 8). This is interpreted to indicate the effect of GBS, which causes further rotation of the grains and increases or decreases the misorientation angles accordingly. Hence the plots of 40–50° (which normally show fairly strong clusters) may be an expression of GBS altering and modifying the Dauphiné twins. Also, when the CPO plots of the parent grain orientations are compared with the neighbour–daughter grain orientations, the neighbour–daughters always show the same pattern of CPO but weaker. This weakening suggests microstructural modification by GBS.

The texture component maps (which illustrate how the orientations of the grains are distributed throughout the microstructure)

show that the neighbour–daughter grains have been moved from being in contact with the parent grain they presumably recrystallised from to being in contact with another parent (Fig. 6). Also the orientations of recrystallised neighbour–daughters have been mixed throughout the matrix. GBS can cause these orientation distribution dispersions through neighbour switching. GBS is a mechanism which is very important for modifying the microstructure with continued strain, causing increases/decreases in the misorientation angles between grains and neighbour switching.

6. Summary and conclusions

Various quartz-rich samples which exhibited deformed microstructures characteristic of dislocation creep regimes 1, 2 and 3 have been quantified using EBSD. The samples were deformed under varying conditions (temperatures of 300–600 °C) and therefore should have experienced different recrystallisation mechanisms. By utilising the EBSD technique to measure the full crystallographic orientation of the parent grains, neighbour–daughters and daughter grains, a detailed analysis of the microstructure has been undertaken.

1. The ratio of subgrain size to recrystallised grain size can be used to constrain the nucleation mechanism for all regimes.
2. Microstructural evidence suggests that SIGBM dominates in regimes 1 and 3, whereas SGR nucleation dominates regime 2.
3. Twinning is an important mechanism for producing HAGBs in all regimes.
4. GBS is required to produce the observed spatial distribution grains in all regimes.
5. GBS is required to construct the displayed range of misorientation angles between grains in all regimes.

Acknowledgements

Bernhard Stöckhert is thanked for providing the Sesia sample. Michael Stipp provided help and advice on how I should perform the collection of my Tonale line samples. Gill Pennock, Sandra Piazolo, Pat Trimby and Richard Law are thanked for their help and stimulating discussions. Also Jan Tullis and Geoff Lloyd are thanked for their review comments, which significantly improved the manuscript. Research was funded by N.E.R.C. studentship grant number NER/A/S/2001/01181.

References

Bailey, J.E., Hirsch, P.B., 1962. The recrystallisation process in some polycrystalline metals. Proceedings of the Royal Society of London 267, 11.
Ball, A., 1997. Superplasticity in the aluminium-zinc eutectoid – An early model revisited. Materials Science and Engineering A 234–236, 365.
Ball, A., Hutchinson, M.M., 1969. Superplasticity in the aluminium-zinc eutectoid. Metal Science Journal 3, 1–7.
Bell, T.H., Etheridge, M.A., 1976. Deformation and recrystallization of quartz in a mylonite zone, central Australia. Tectonophysics 32, 235–267.
Bestmann, M., Habler, G., Heidelbach, F., Thöni, M., 2008. Dynamic recrystallization of garnet and related diffusion processes. Journal of Structural Geology 30, 777–790.
Bestmann, M., Prior, D.J., 2003. Intragranular dynamic recrystallization in naturally deformed calcite marble: diffusion accommodated grain boundary sliding as a result of subgrain rotation recrystallization. Journal of Structural Geology 25, 1597–1613.
Callaway, C., 1884. Notes on progressive metamorphism. Geological Magazine 1, 218–224.
Etheridge, M.A., Hobbs, B.E., 1974. Chemical and deformational controls on recrystallization of mica. Contributions to Mineralogy and Petrology 43, 111–124.
Friedel, G., 1923. Sur les macles du quartz. Bulletin de la Société Française de Minéralogie et de Crystallographie 46, 79–95.
Gifkins, R.C., 1976. Grain-boundary sliding and its accommodation during creep and superplasticity. Metallurgical Transactions A – Physical Metallurgy and Materials Science 7, 1225–1232.
Guillope, M., Poirier, J.P., 1979. Dynamic recrystallisation during creep of single-crystalline halite: an experimental study. Journal of Geophysical Research 84, 5557–5567.
Halfpenny, A., 2010. Some important practical issues for collection and manipulation of electron backscatter diffraction (EBSD) data from rocks and minerals. Journal of the Virtual Explorer 35 (3).
Halfpenny, A., Prior, D.J., Wheeler, J., 2006. Analysis of dynamic recrystallization and nucleation in a quartzite mylonite. Tectonophysics 427, 3–14.
Halfpenny, A., Prior, D.J., Wheeler, J., 2004. Using electron backscatter diffraction (EBSD) to measure misorientation between 'parent' and 'daughter' grains. Implications for recrystallisation and nucleation. In: Recrystallization and Grain Growth, Pts 1 and 2. Trans Tech Publications LTD, pp. 573–578.
Hall, E.O., 1951. The deformation and ageing of mild steel: 3. Discussion of results. Proceedings of the Physical Society of London Section B 64, 747–753.
Heitzmann, P., 1987. Evidence of late Oligocene early Miocene backthrusting in the central Alpine root zone. Geodinamica Acta 1, 183–192.
Hirth, G., Tullis, J., 1992. Dislocation creep regimes in quartz aggregates. Journal of Structural Geology 14, 145–159.
Hobbs, B.E., 1968. Recrystallization of single crystals of quartz. Tectonophysics 6, 353–401.
Jiang, Z.T., Prior, D.J., Wheeler, J., 2000. Albite crystallographic preferred orientation and grain misorientation distribution in a low-grade mylonite: implications for granular flow. Journal of Structural Geology 22, 1663–1674.
Kruhl, J.H., Peternell, M., 2002. The equilibration of high-angle grain boundaries in dynamically recrystallised quartz: the effect of crystallography and temperature. Journal of Structural Geology 24, 1125–1137.
Kuster, M., Stockhert, B., 1999. High differential stress and sublithostatic pore fluid pressure in the ductile regime – microstructural evidence for short-term post-seismic creep in the Sesia Zone, Western Alps. Tectonophysics 303, 263–277.
Law, R.D., 1987. Heterogeneous deformation and quartz crystallographic fabric transitions: natural examples from the Moine Thrust Zone at the Stack of Glencoul, Northern Assynt. Journal of Structural Geology 9, 819–833.
Law, R.D., Casey, M., Knipe, R.J., 1986. Kinematic and tectonic significance of microstructures and crystallographic fabrics within quartz mylonites from the Assynt and Eriboll regions of the Moine Thrust Zone, NW Scotland. Transactions of the Royal Society of Edinburgh 77, 99–125.
Law, R.D., Mainprice, D., Casey, M., Lloyd, G.E., Knipe, R.J., Cook, B., Thigpen, J.R., 2010. Moine Thrust Zone mylonites at the Stack of Glencoul; I, microstructures, strain and influence of recrystallization on quartz crystal fabric development. Geological Society Special Publications 335, 543–577.
Lloyd, G.E., 1987. Atomic-number and crystallographic contrast images with the SEM – A review of backscattered electron techniques. Mineralogical Magazine 51, 3–19.
Lloyd, G.E., Freeman, B., 1994. Dynamic recrystallization of quartz under greenschist conditions. Journal of Structural Geology 16, 867–881.
Lloyd, G.E., Law, R.D., Mainprice, D., 2010. Predicting seismic properties from three-dimensional microstructures – A new look at an old quartzite. Geological Society Special Publications 335, 603–662.
Mariani, E., Mecklenburgh, J., Wheeler, J., Prior, D.J., Heidelbach, F., 2009. Microstructure evolution and recrystallization during creep of MgO single crystals. Acta Materialia 57, 1886–1898.
McLaren, A.C., 1986. Some speculations on the nature of high-angle grain boundaries in quartz rocks. Geophysical Monograph 36, 233–245.
Menegon, L., Piazolo, S., Pennacchioni, G., 2011. The effect of Dauphine twinning on plastic strain in quartz. Contributions to Mineralogy and Petrology/Beitrage zur Minerologie und Petrologie. Berlin and New York NY 161, 635–652.
Mohamed, F.A., Langdon, T.G., 1976. Deformation mechanism maps for superplastic materials. Scripta Metallurgica 10, 759.
Ord, A., Christie, J.M., 1984. Flow stresses from microstructures in mylonitic quartzites of the Moine Thrust Zone, Assynt area, Scotland. Journal of Structural Geology 6, 639–654.
Pennock, G.M., Drury, M.R., Peach, C.J., Spiers, C.J., 2006. The influence of water on deformation microstructures and textures in synthetic NaCl measured using EBSD. Journal of Structural Geology 28, 588.
Petch, N.J., 1953. The cleavage strength of polycrystals. Journal of the Iron and Steel Institute 174, 25–28.
Poirier, J.P., Guillope, M., 1979. Deformation induced recrystallization of minerals. Bulletin De Mineralogie 102, 67–74.
Prior, D.J., Bestmann, M., Halfpenny, A., Mariani, E., Piazolo, S., Tullis, J., Wheeler, J., 2004. Recrystallization and grain growth in rocks and minerals. In: Recrystallization and Grain Growth, Pts 1 and 2. Trans Tech Publications LTD, pp. 545–550.
Prior, D.J., Boyle, A.P., Brenker, F., Cheadle, M.C., Day, A., Lopez, G., Peruzzo, L., Potts, G.J., Reddy, S., Spiess, R., Timms, N.E., Trimby, P., Wheeler, J., Zetterstrom, L., 1999. The application of electron backscatter diffraction and orientation contrast imaging in the SEM to textural problems in rocks. American Mineralogist 84, 1741–1759.
Prior, D.J., Mariani, E., Wheeler, J., 2009. EBSD in the earth sciences: applications, common practice and challenges. In: Schwartz, A.J., Kumar, M., Adams, B.L., Field, D.P. (Eds.), Electron Backscatter Diffraction in Materials Science. Springer Science + Business Media, pp. 345–360.
Prior, D.J., Trimby, P.W., Weber, U.D., Dingley, D.J., 1996. Orientation contrast imaging of microstructures in rocks using forescatter detectors in the scanning electron microscope. Mineralogical Magazine 60, 859–869.

Schmid, S.M., Aebli, H.R., Heller, F., Zingg, A., 1989. The role of the Pedriatic Line in the tectonic evolution of the Alps. Geological Society Special Publications 45, 153–171.
Schmid, S.M., Casey, M., Starkey, J., 1986. Complete fabric analysis of some commonly observed quartz c-axis patterns. Geophysical Monograph 36, 263–286.
Schmidt, N.H., Olesen, N.O., 1989. Computer-aided determination of crystal-lattice orientation from electron-channeling patterns in the SEM. Canadian Mineralogist 27, 15–22.
Shigematsu, N., Prior, D.J., Wheeler, J., 2006. First combined electron backscatter diffraction and transmission electron microscopy study of grain boundary structure of deformed quartzite. Journal of Microscopy 224, 306–321.
Skemer, P., Karato, S.I., 2008. Sheared lherzolite xenoliths revisited. Journal of Geophysical Research – Solid Earth 113.
Stipp, M., Fugenschuh, B., Gromet, L.P., Stunitz, H., Schmid, S.M., 2004. Contemporaneous plutonism and strike-slip faulting: a case study from the Tonale fault zone north of the Adamello pluton (Italian Alps). Tectonics 23.
Stipp, M., Kunze, K., 2008. Dynamic recrystallization near the brittle-plastic transition in naturally and experimentally deformed quartz aggregates. Tectonophysics 448, 77–97.
Stipp, M., Schmid, S., 1998. Evidence for the contemporaneity of movements along the Tonale Line and the intrusion of parts of the Adamello batholith. Memorie di Scienze Geologiche 50, 89–90.
Stipp, M., Stunitz, H., Heilbronner, R., Schmid, S.M., 2002a. Dynamic recrystallisation of quartz: correlation between natural and experimental conditions. Geological Society Special Publications 200, 171–190.
Stipp, M., Stunitz, H., Heilbronner, R., Schmid, S.M., 2002b. The eastern Tonale fault zone: a 'natural laboratory' for crystal plastic deformation of quartz over a temperature range from 250 to 700 degrees C. Journal of Structural Geology 24, 1861–1884.
Stipp, M., Tullis, J., 2003. The recrystallized grain size piezometer for quartz. Geophysical Research Letters 30.
Stipp, M., Tullis, J., Scherwath, M., Behrmann, J., 2010. A new perspective on paleopiezometry: dynamically recrystallized grain size distributions indicate mechanism changes. Geology 38, 759–762.
Storey, C.D., Prior, D.J., 2005. Plastic deformation and recrystallization of garnet: a mechanism to facilitate diffusion creep. Journal of Petrology 46, 2593–2613.
Trepmann, C., Stockhert, B., 2001. Mechanical twinning of jadeite – An indication of synseismic loading beneath the brittle-plastic transition. International Journal of Earth Sciences 90, 4–13.
Trepmann, C.A., Stockhert, B., 2002. Cataclastic deformation of garnet: a record of synseismic loading and postseismic creep. Journal of Structural Geology 24, 1845–1856.
Trepmann, C.A., Stockhert, B., 2003. Quartz microstructures developed during non-steady state plastic flow at rapidly decaying stress and strain rate. Journal of Structural Geology 25, 2035–2051.
Trimby, P.W., Prior, D.J., Wheeler, J., 1998. Grain boundary hierarchy development in a quartz mylonite. Journal of Structural Geology 20, 917–935.
Tullis, J., DellAngelo, L.N., Yund, R., 1990. Ductile shear zones from brittle precursors in feldspathic rocks: the role of dynamic recrystallization. Geophysical Monograph 56, 67–81.
Twiss, R.J., 1986. Variable sensitivity piezometric equations for dislocation density and subgrain diameter and their relevance to olivine and quartz. Geophysical Monograph 36, 247–261.
Urai, J.L., Means, W.D., Lister, G.S., 1986. Dynamic recrystallisation of minerals. Geophysical Monograph 36, 161–200.
Valcke, S.L.A., Pennock, G.M., Drury, M., De Bresser, J.H.P., 2006. Electron backscattered diffraction as a tool to quantify subgrains in deformed calcite. Journal of Microscopy 224, 264–276.
Vernooij, M.G.C., den Brok, B., Kunze, K., 2006a. Development of crystallographic preferred orientations by nucleation and growth of new grains in experimentally deformed quartz single crystals. Tectonophysics 427, 35–53.
Vernooij, M.G.C., Kunze, K., den Brok, B., 2006b. 'Brittle' shear zones in experimentally deformed quartz single crystals. Journal of Structural Geology 28, 1292.
Wheeler, J., Jiang, Z., Prior, D.J., Tullis, J., Drury, M.R., Trimby, P.W., 2003. From geometry to dynamics of microstructure: using boundary lengths to quantify boundary misorientations and anisotropy. Tectonophysics 376, 19–35.
Wheeler, J., Prior, D.J., Jiang, Z., Spiess, R., Trimby, P.W., 2001. The petrological significance of misorientations between grains. Contributions to Mineralogy and Petrology 141, 109–124.
White, S., 1976. Effects of strain on microstructures, fabrics, and deformation mechanisms in quartzites. Philosophical Transactions of the Royal Society of London. Series A, Mathematical and Physical Sciences 283, 69–86.
White, S., 1977. Geological significance of recovery and recrystallization processes in quartz. Tectonophysics 39, 143–170.
White, S., 1979. Grain and sub-grain size variations across a mylonite zone. Contributions to Mineralogy and Petrology 70, 193–202.
Zhang, Y., Hobbs, B.E., Jessell, M.W., 1994. The effect of grain-boundary sliding on fabric development in polycrystalline aggregates. Journal of Structural Geology 16, 1315–1325.
Zhang, Y., Jessell, M.W., Hobbs, B.E., 1996. Experimental and numerical studies of the accommodation of strain incompatibility on the grain scale. Journal of Structural Geology 18, 451–460.